VII. COLLIDER STORAGE RING

A. Introduction

After one μ^+ bunch and one μ^- bunch have been accelerated to collision energy, the two bunches are injected into the collider ring, which is a fixed field storage ring. Parameters for several possible collider storage rings are given in table I. Collider ring lattices have been developed for two of the collision energies in this table: 100 GeV and 3 TeV in the center of mass.

Three operational modes are proposed in the above table for the 100 GeV collider, each requiring different machine optics. The following sections discuss a 100 GeV collider lattice for two of the modes, the broad momentum spread case ($\Delta p/p$ of 0.12%, rms) and the narrow momentum spread case ($\Delta p/p$ of 0.003%), as well as a 3 TeV collider lattice.

B. Collider Lattices

1. Design criteria

Stringent criteria have been imposed on the collider lattice designs in order to attain the specified luminosities. The first and most difficult criterion to satisfy is provision of an Interaction Region (IR) with extremely low β^* values at the collision point consistent with acceptable dynamic aperture. The required β^* values for the 100 GeV collider are 4 cm for the broad momentum spread case and 14 cm for the narrow momentum spread case. For the 3 TeV machine, β^* is only 3 mm. These β^* values were tailored to match the longitudinal bunch lengths in order to avoid luminosity dilution from the hour-glass effect. Achieving this requirement in the 3 TeV lattice is complicated by the high peak beta function values in the final focus quadrupoles requiring 8-10 cm radial apertures. The correspondingly weakened gradients combined with the ultra-high energy make for a long final focus structure. (In contrast, the lower energy and larger β^* values in the 100 GeV collider lead to an efficient, compact final focus telescope.) Compounding the problem, particularly for the 3 TeV design, is the need to protect the superconducting coils from the decay products of the muons. Placing a tungsten shield between the vacuum chamber and the coils can increase the radial aperture in the 3 TeV quadrupoles by as much as 6 cm, lowering available gradients still further. Final focus designs must also include collimators and background sweep dipoles, and other provisions for protecting the magnets and detectors from muon decay electrons. Effective schemes have been incorporated into the current lattices.

Another difficult constraint imposed on the lattice is that of isochronicity. A high degree of isochronicity is required in order to maintain the short bunch structure without excessive rf voltage. In the lattices presented here, control over the momentum compaction is achieved through appropriate design of the arcs.

A final criterion especially important in the lower energy colliders is that the ring circumference be as small as feasible in order to minimize luminosity degradation through decay of the muons. Achieving small circumference requires high fields in the bending magnets as well as a compact, high dipole packing fraction design. To meet the small circumference demand, 8 T pole tip fields have been assumed for all superconducting magnets, with the exception of the 3 TeV final focus quadrupoles, whose pole tips are assumed to be as high as 12 T. In addition, design studies for still higher field dipoles are in progress.

2. rf system

The rf requirements depend on the momentum compaction of the lattice and on the parameters of the muon bunch. For the case of very low momentum spread, synchrotron motion is negligible and the rf system is used solely to correct an energy spread generated through the impedance of the machine. For the cases of higher momentum spreads, there are two approaches. One is to make the momentum compaction zero to high order through lattice design. Then the synchrotron motion can be eliminated, and the rf is again only needed to compensate the induced energy spread correction. Alternatively, if some momentum compaction is retained, then a more powerful rf system is needed to maintain the specified short bunches. In either case, rf quadrupoles will be required to generate BNS [188,189] damping of the transverse head-tail instability.

3. 3 TeV CoM lattice

The 3 TeV ring has a roughly racetrack design with two circular arcs separated by an experimental insertion on one side, and a utility insertion for injection, extraction, and beam scraping on the other. The experimental insertion includes the interaction region (IR) followed by a local chromatic correction section (CCS) and a matching section. The chromatic correction section is optimized to correct the ring's linear chromaticity, which is mostly generated by the low beta quadrupoles in the IR. In designs of e^+e^- colliders, it has been found that local chromatic correction of the final focus is essential [190–193], as was found to be the case here. The 3 TeV IR and CCS are displayed in Fig. 41. The accompanying 3 TeV arc module in Fig 42 is an example of a module which controls momentum compaction (i.e. isochronicity) of the entire ring.

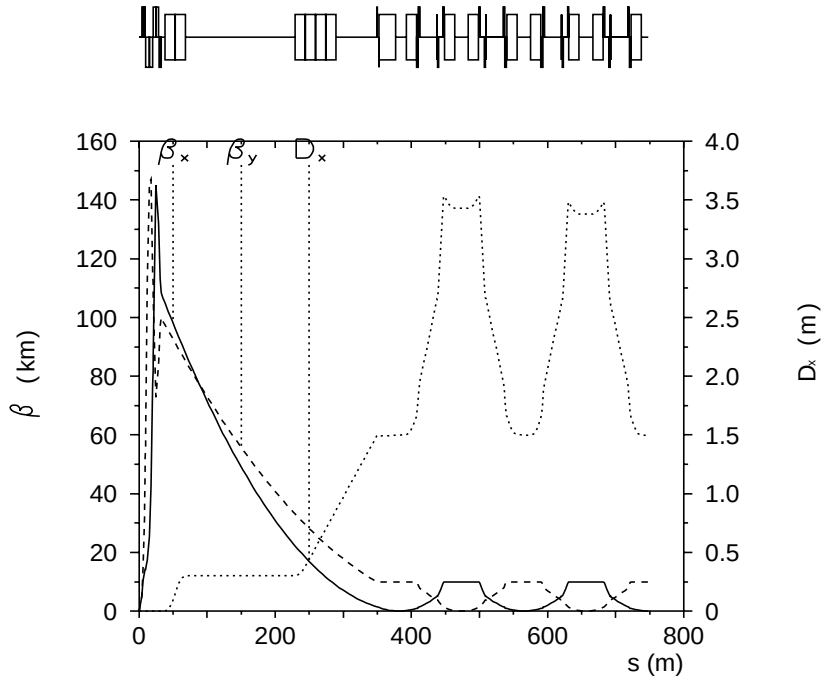

FIG. 41. Example (a): 3 TeV IR and chromatic correction section.

4. 100 GeV CoM lattices

For the 100 GeV CoM collider [194], two operating modes are contemplated: a high luminosity case with broad momentum acceptance to accommodate a beam with a $\Delta p/p$ of $\pm 0.12\%$ (rms), and one with a much narrower momentum acceptance and lower luminosity for a beam with $\Delta p/p$ of $\pm 0.003\%$ (rms). For the broad momentum acceptance case, β^* must be 4 cm and for the narrow momentum acceptance case, 14 cm. In either case, the bunch length must be held comparable to the value of β^*. The 100 GeV ring geometry is highly compact and more complicated than a racetrack, but the lattice has regions with the same functions as those of the 3 TeV ring.

Two independent 100 GeV lattice designs have evolved; these are described below in separate sections and denoted Example (a) and Example (b), respectively. The first design described is a lattice which has two optics modes. In the high luminosity mode, the β^* value is 4 cm with a transverse and momentum aperture sufficient to accept a normalized beam emittance of 90π (rms) and a $\Delta p/p$ of $\pm 0.12\%$ (rms). The second, lower luminosity mode has a

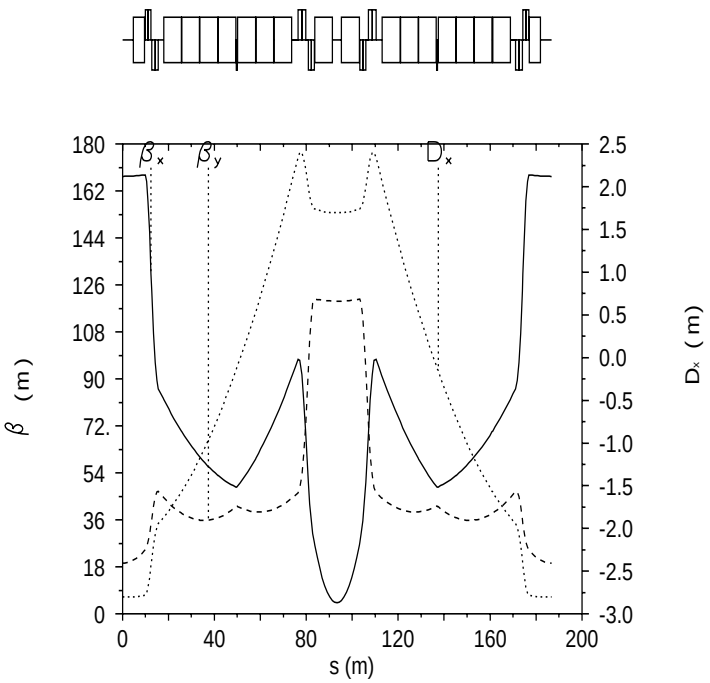

FIG. 42. Example (a): 3 TeV arc module.

β^* value of 14 cm with a very large transverse acceptance, but small, approximately monochromatic, momentum acceptance.

The second 100 GeV lattice described is another collider design with a 4 cm β^* optics mode. Although the number of magnets differ between the two lattices, the most important optics difference between the two is in the modules used in the arcs.

5. 100 GeV CoM. Example (a)

The need for different collision modes in the 100 GeV machine led to an Interaction Region design with two optics modes: one with broad momentum acceptance ($\Delta p/p$ of 0.12%, rms) and a collision β^* of 4 cm, and the other basically monochromatic ($\Delta p/p$ of 0.003%, rms) and a larger collision β^* of 14 cm. The first lattice design, denoted Example (a), shown in Fig. 43 and Fig. 44, has a total circumference of about 350 m with arc modules accounting for only about a quarter of the ring circumference.

The low beta function values at the IP are mainly produced by three strong superconducting quadrupoles in the Final Focus Telescope (FFT) with pole tip fields of 8 T. The full interaction region is symmetric under reflection about the interaction point (IP). Because of significant, large angle backgrounds from muon decay, a background sweep dipole is included in the final focus telescope and placed near the IP to protect the detector and the low β quadrupoles [195]. It was found that this sweep dipole, 2.5 m long with an 8 T field, provides sufficient background suppression. The first quadrupole is located 5 m away from the interaction point, and the beta functions reach a maximum value of 1.5 km in the final focus telescope, when the maxima of the beta functions in both planes are equalized. For this maximum beta value, the quadrupole apertures must be at least 11 cm in radius to accommodate 5 σ of a 90 π mm-mrad, 50 GeV muon beam (normalized rms emittance) plus a 2 to 3 cm thick tungsten liner [196]. The natural chromaticity of this interaction region is about -60.

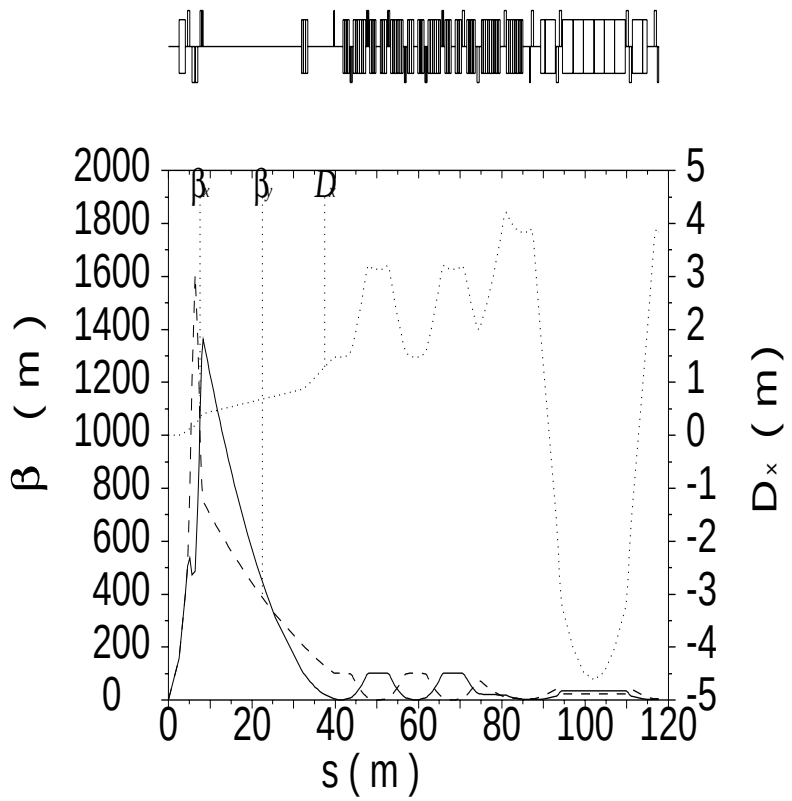

FIG. 43. Example (a): 4 cm β^* Mode showing half of the IR, local chromatic correction section and one of three arc modules.

Local chromatic correction of the muon collider interaction region is required to achieve broad momentum acceptance. The basic approach developed by Brown [191] and others [197], is implemented in the Chromatic Correction Region (CC). The CC contains two pairs of sextupoles, one pair for each transverse plane, all located at locations with high dispersion. The sextupoles of each pair are located at positions of equal, high beta value in the plane (horizontal or vertical) whose chromaticity is to be corrected, and very low beta waist in the other plane. Moreover, the two sextupoles of each pair are separated by a betatron phase advance of near π, and each sextupole has a phase separation of $(2n+1)\frac{\pi}{2}$ from the IP, where n is an integer. The result of this arrangement is that the geometric aberrations of each sextupole is canceled by its companion while the chromaticity corrections add.

The sextupoles of each pair are centered about a minimum in the opposite plane ($\beta_{min} < 1m$), which provides chromatic correction with minimal cross correlation between the planes. A further advantage to locating the opposite plane's minimum at the center of the sextupole, is that this point is $\frac{\pi}{2}$ away from, or "out of phase" with, the source of chromatic effects in the final focus quadrupoles; i.e the plane not being chromatically corrected is treated like the IP in terms of phase to eliminate a second order chromatic aberration generated by an "opposite-plane" sextupole.

In this lattice example, the CC (Fig. 45) was optimized to be as short as possible. The $\beta_{\rm max}$ is only 100 m and the $\beta_{\rm min} = 0.7$ m, giving a $\beta_{\rm ratio}$ between planes of about 150, so the dynamic aperture is not compromised by a large amplitude dependent tuneshift.

This large beta ratio, combined with the opposite plane phasing, allows the sextupoles for the opposite planes to be interleaved, without significantly increasing the nonlinearity of the lattice. In fact, interleaving improved lattice performance compared to that of a non-interleaved correction scheme, due to a shortening of the chromatic correction section, which lowers its chromaticity contribution [198]. The use of somewhat shallower beta minima with less variation in beta through the sextupoles was made to soften the chromatic aberrations, although this caused a slight violation of the exact π phase advance separation between sextupole partners. The retention of an exact π phase advance difference between sextupoles was found to be less important to the dynamic aperture than elimination of minima with $\beta_{\rm min} < 0.5$ m.

The total momentum compaction contributions of the IR, CC, and matching sections is about 0.04. The total length

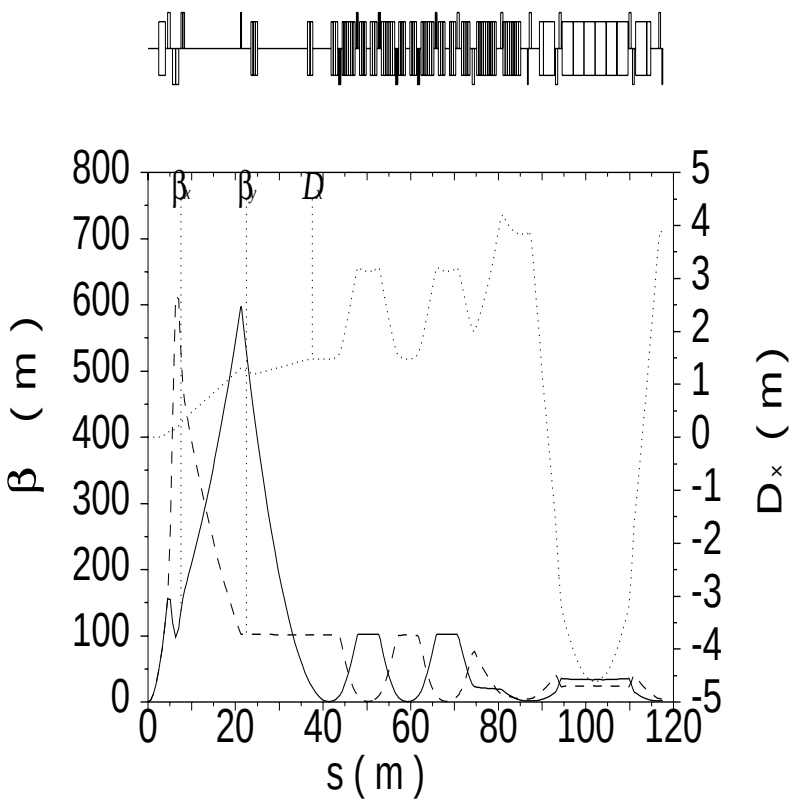

FIG. 44. Example (a): 14 cm β^* Mode showing half of the IR, local chromatic correction, and one of three arc modules.

of these parts is 173 m, while that of the the momentum compaction correcting arc is 93 m. From these numbers, it follows that this arc must have a negative momentum compaction of about -0.09 in order to offset the positive contributions from the rest of the ring.

The arc module is shown in Fig. 46. It has the small beta functions characteristic of FODO cells, yet a large, almost separate, variability in the momentum compaction of the module which is a characteristic associated with the flexible momentum compaction module [199,200]. The small beta functions are achieved through the use of a doublet focusing structure which produces a low beta simultaneously in both planes. At the dual minima, a strong focusing quadrupole is placed to control the derivative of dispersion with little impact on the beta functions. Negative values of momentum compaction as low as $\alpha = -0.13$ have been achieved, and $\gamma_t = 2\ i$, has been achieved with modest values of the beta function.

This arc module was able to generate the needed negative momentum compaction with beta functions of 40 m or less.

A very preliminary calculation of the dynamic aperture [198] without optimization of the lattice or inclusion of errors and end effects is given in Fig. 47. One would expect that simply turning off the chromatic correction sextupoles in the 4 cm β^* mode would result in a linear lattice with a large transverse aperture. With only linear elements, the 4 cm β^* optics was found to be strongly nonlinear with limited on-momentum dynamic acceptance.

A normal form analysis using COSY INFINITY [201] showed that the variation of tune shift with amplitude was large, which was the source of the strong nonlinearity in the seemingly linear lattice. To locate the source of this nonlinearity, a lattice consisting of the original IR and arcs only (no CC), was studied. Numerical studies confirmed similar dynamic aperture and variation of tune shift with amplitude. This ruled out the possibility that the dynamic aperture was limited by the low beta points in the local chromatic correction section and points to the IR as the source of the nonlinearity. These findings were also verified [202] using a Runge-Kutta integrator to track through the IR and a linear matrix for the rest of the lattice. Further analytical study using perturbation theory showed that the first order contribution to the tune shift with amplitude is proportional to $\gamma_{x,y}^2$ and $\gamma_x\gamma_y$, which are large in this IR. These terms come from the nonlinear terms of p_x/p_0 and p_y/p_0, which, to first order, equal the angular divergence of

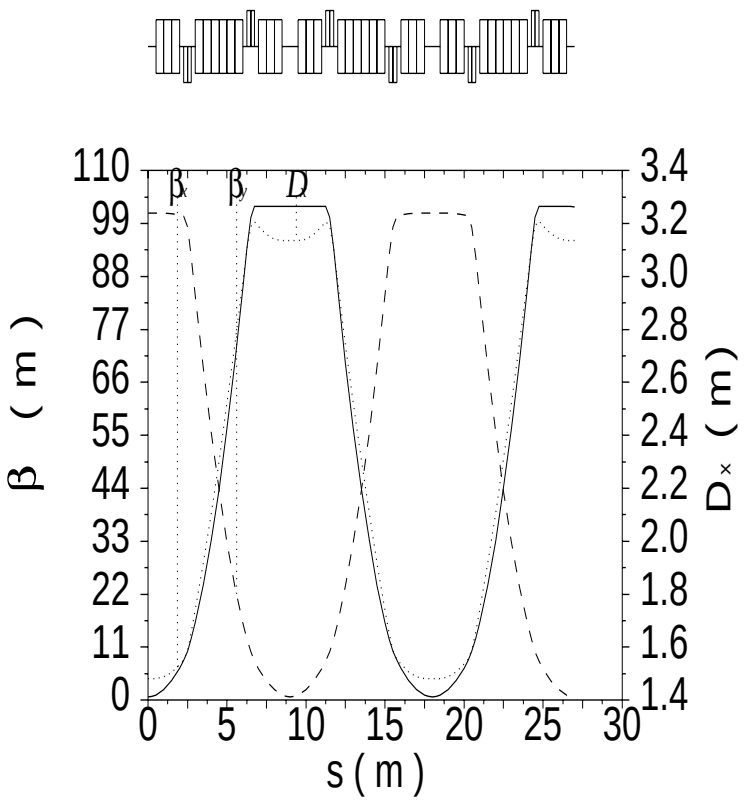

FIG. 45. Example (a): The chromatic correction module.

a particle. As a demonstration, a comparison to the LHC low beta IR was done. Taking into account only the drift from the IP to the first quadrupole, the horizontal detuning at 10σ of the present IR ($\beta^* = 4$ cm) is 0.01, whereas the detuning of the entire LHC lattice is below 1E-4. This also explains the fact that the on-momentum aperture of the wide momentum spread mode remains roughly constant despite various versions and correction attempts.

It was therefore concluded and later shown that the dynamic aperture of the more relaxed β^* of 14 cm would not have the same strong nonlinearities due to the reduced angular terms. In fact, the variation of tune shift with amplitude was less by an order of magnitude; hence the large transverse acceptance shown in Fig. 47 (dashed).

6. 100 GeV CoM. Example (b)

The second lattice design, Example (b), is shown in Fig. 48 starting from the IP. The 1.5 m background clearing dipole is 2.5 m away from the IP and is followed by the triplet quadrupoles with the focusing quadrupole in the center. The interaction region (IR) stops at about 24 m from the IP. Because of the small low betatron functions in both transverse planes, the betatron functions at the final focusing triplets increase to ~ 1550 m. The natural chromaticities, of order ~ -40, are high, requiring local correction. Due to the size limitation of the collider ring, it appears that we have room for only two pairs of interleaved sextupoles on each side of the IP, each pair correcting chromaticity in one transverse plane. The correction section on each side of the IP spans a distance of roughly 61.3 m.

The SX1's are the two horizontal correction sextupoles. They should be placed at positions with the same betatron functions and dispersion function, and separated horizontally and vertically by phase advances $\Delta\psi_x$ and $\Delta\psi_y = \pi$ so that their nonlinear effect will be confined in the region between the two sextupoles. Their horizontal phase advances should also be integral numbers of π from the triplet focusing F-quadrupole so that the chromaticity compensation for that quadrupole will be most efficient [197]. The SX2's are the two vertical correction sextupoles which should be placed similarly at designated locations. In general, it will be difficult to satisfy all the requirements mentioned;

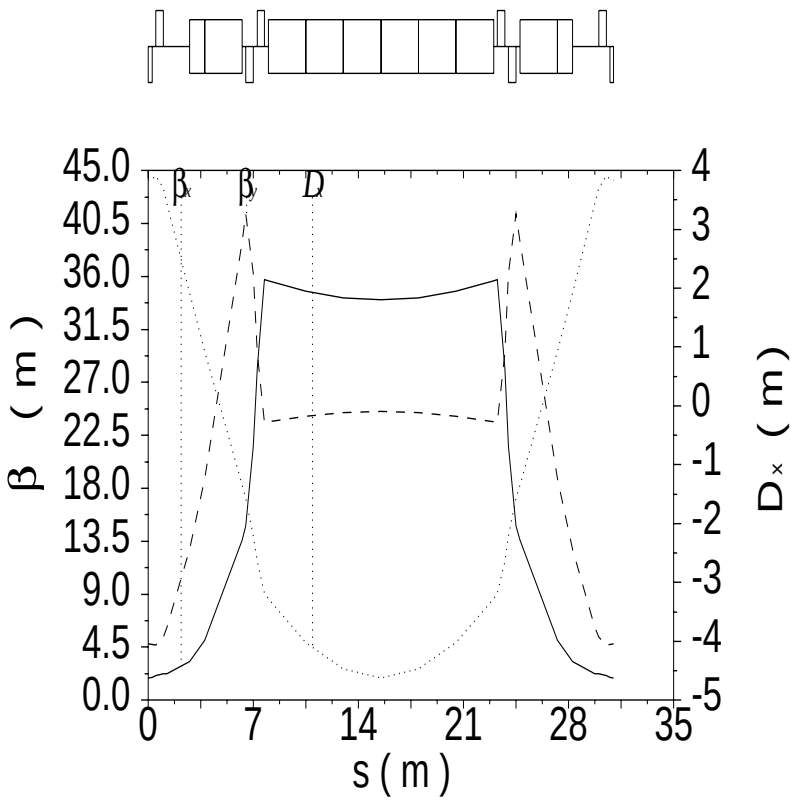

FIG. 46. Example (a): A flexible momentum compaction arc module.

especially in this situation, luminosity arguments limit the lattice size. For this lattice, the Twiss properties at the centers of the four correction sextupoles are listed in table XII, where all the figures given by the lattice code are displayed. An attempt was made to satisfy all the requirements at the expense of having $\Delta\psi_y/(2\pi) = 0.60$ instead of 0.50 for the SX1's. This trade-off is explained below.

TABLE XII. Twiss properties of the IR correction sextupoles.

	Distance	Phase Advances		Betatron Functions (m)		Dispersion
	(m)	$\psi_x/(2\pi)$	$\psi_y/(2\pi)$	β_x	β_y	(m)
SX2	33.5061	0.48826	0.74953	1.00000	100.00012	2.37647
SX2	62.3942	0.98707	1.24953	1.00000	100.00009	2.37651
SX1	49.3327	0.74892	0.87703	100.00023	1.00000	2.66039
SX1	74.6074	1.24892	1.47987	99.99967	0.99992	2.65817

The second order effects of the sextupoles contribute to the amplitude dependent tune spreads, which, if too large, can encompass resonances leading to dynamical aperture limitation. For example, in this lattice,

$$\begin{aligned} \nu_x &= 8.126337 - \ 100\ \epsilon_x - \ 4140\ \epsilon_y, \\ \nu_y &= 6.239988 - 4140\ \epsilon_x - \ 54.6\ \epsilon_y, \end{aligned} \tag{28}$$

where ϵ_x and ϵ_y are the horizontal and vertical unnormalized emittances in πm. In order to eliminate these tune spreads due to the sextupole nonlinearity, the sufficient conditions are [203]:

$$\sum_k \frac{S_k e^{i\psi_{xk}}}{\sin \pi\nu_x} = 0\,, \qquad \sum_k \frac{S_k e^{i3\psi_{xk}}}{\sin 3\pi\nu_x} = 0\,,$$

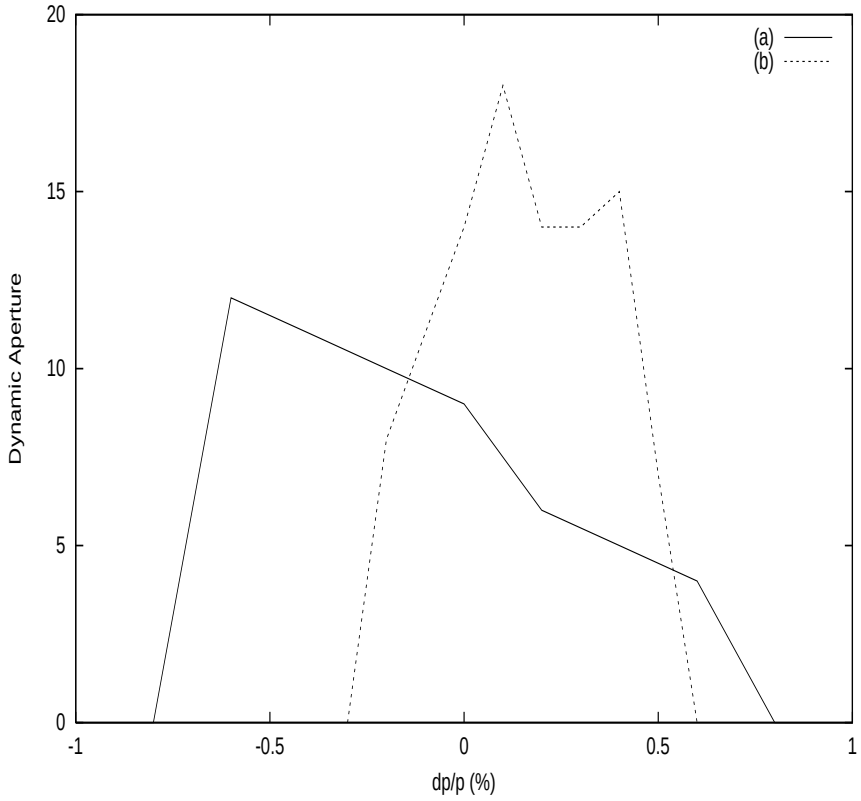

FIG. 47. Example (a): A preliminary dynamic aperture for the 4 cm β^* mode where $\sigma_{\rm rms} = 82\ \mu m$ (solid) and the 14 cm β^* mode where $\sigma_{\rm rms} = 281\ \mu m$ (dashed).

$$\sum_k \frac{\bar{S}_k e^{i\psi_{xk}}}{\sin \pi\nu_x} = 0\,, \qquad \sum_k \frac{\bar{S}_k e^{i\psi_{\pm k}}}{\sin \pi\nu_\pm} = 0\,, \tag{29}$$

where for the kth thin normal sextupole with strength $S_{Nk} = \lim_{\ell\to 0} [B''\ell/(B\rho)]_k$,

$$S_k = \left[S_{_N}\beta_x^{3/2}\right]_k\,, \quad \bar{S}_k = \left[S_{_N}\beta_x^{1/2}\beta_y\right]_k\,, \tag{30}$$

$\psi_{\pm k} = (2\psi_y \pm \psi_x)_k$, and $\nu_{\pm k} = (2\nu_y \pm \nu_x)_k$. The 5 requirements come about because there are 5 first order resonances driven by the sextupoles when the residual tunes of the ring satisfy $[3\nu_x] = 0$, $[\nu_\pm] = 0$ and two $[\nu_x] = 0$. The nominal tunes shown in Eq. (28) are far from these resonances. Therefore, the sines in the denominators of Eq. (29) can be omitted in this discussion. Since the strengths of SX1 and SX2 are similar, we have $S_{\rm SX2} \ll \bar{S}_{\rm SX1} \ll \bar{S}_{\rm SX2} \ll S_{\rm SX1}$. In fact, they are roughly in the ratios of $1 : (\beta_{\rm max}/\beta_{\rm min})^{1/2} : \beta_{\rm max}/\beta_{\rm min} : (\beta_{\rm max}/\beta_{\rm min})^{3/2}$, which amount roughly to 1:10:100:1000 in this lattice. In above, $\beta_{\rm max}$ represents either β_x at the SX1's or β_y at the SX2's, and $\beta_{\rm min}$ represents either β_y at the SX1's or β_x at the SX2's. Thus, the first two restrictions in Eq. (29) are the most important, implying that all $\beta_{\rm max}$ and $\beta_{\rm min}$ for each pair of SX1's must be made equal and $\Delta\psi_x = \pi$ between them must be strictly obeyed. The third restriction is the next important one, for which $\bar{S}_{\rm SX2}$ must be made equal for each pair of SX2's and their horizontal phase difference must equal π. The only two parameters left are $\Delta\psi_y$ between a pair of SX1's and $\Delta\psi_y$ between a pair of SX2's. They affect the restrictions for the $\nu_\pm$ resonances only, where the effective sextupole strengths $\bar{S}_{\rm SX1}$ and $\bar{S}_{\rm SX2}$ are involved. Thus if we allow one restriction to be relaxed, the relaxation of $\Delta\psi_y = \pi$ for the SX1's will be least harmful.

Flexible momentum compaction (FMC) modules [200] are used in the arc. The momentum compaction of the arc has to be made negative in order to cancel the positive momentum compaction of the IR, so that the whole ring becomes quasi-isochronous. This is accomplished in three ways: 1) removing the central dipole of the usual FMC module; 2) increasing the length of the first and last dipoles, and 3) increasing the negative dispersion at the entrance.

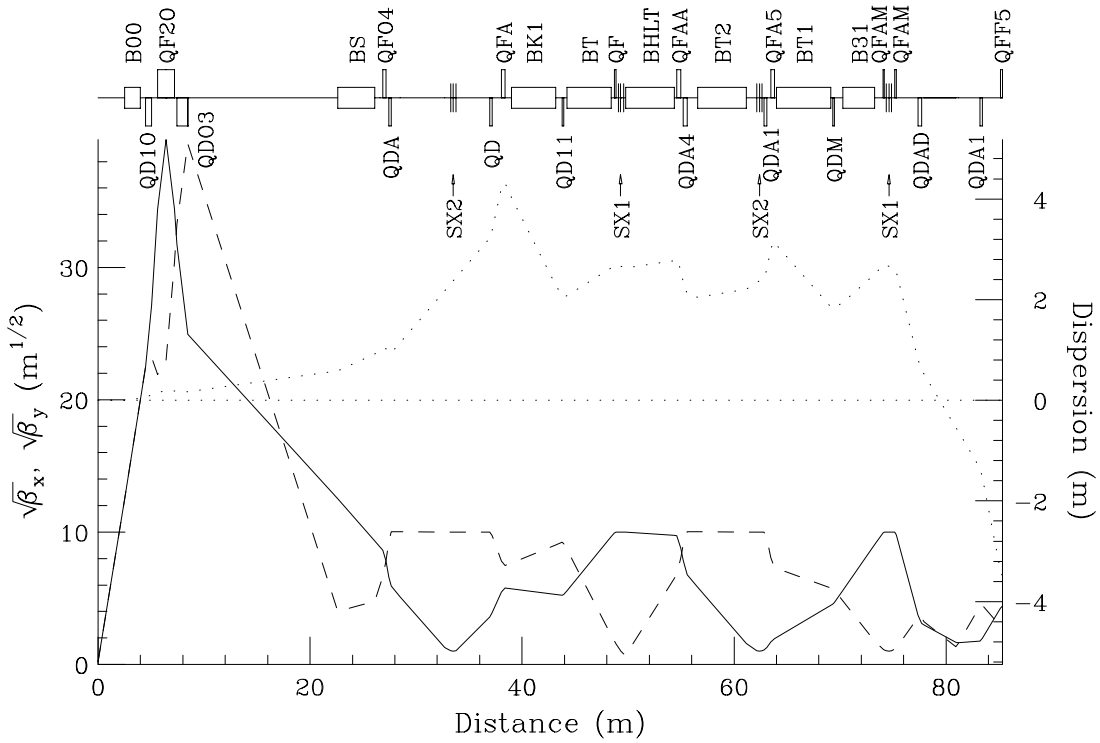

FIG. 48. Example (b): Lattice structure of the IR including local chromaticity corrections. β_x (solid); β_y (dashed); dispersion (dotted). The maximum and minimum β_x are 1571.74 and 0.040 m, the maximum and minimum β_y are 1550.94 and 0.040 m, while the maximum and minimum dispersions are 4.31 and -3.50 m. The natural horizontal and vertical chromaticities are -41.46 and -39.90, giving a transition gamma of $\gamma_t = 5.52$. The total module length is 85.32 m with a total bend angle of 1.307 rad.

Two such modules will be required for half of the collider ring, one of which is shown in Fig. 49. To close the ring geometrically, there will be a ~ 72.0 m straight section between the two sets of FMC modules. The total length of the collider ring is now only $C = 354.3$ m. This is a nice feature, since a small ring allows a larger number of collisions before the muons decay appreciably. Note that the IR and local correction sections take up 48.2% of the whole ring. The momentum compaction factor of this ring is now $\alpha_0 = -2.77 \times 10^{-4}$. The rf voltage required to maintain a bunch with rms length σ_ℓ and rms momentum spread σ_δ is $V_{\rm rf} = |\eta| E C^2 \sigma_\delta^2 / (2\pi h \sigma_\ell^2)$, where η is the slippage factor and E the muon energy. On the other hand, if the bucket height is taken as k times the rms momentum spread of the bunch, the rf harmonic is given by $h = C/(k\pi\sigma_\ell)$. Thus, for $\sigma_\ell = 4$ cm and $\sigma_\delta = 0.0012$, this lattice requires an rf voltage of $V_{\rm rf} \approx 88k$ kV. Since α_0 is negative already, its absolute value can be further lowered easily if needed. However, we must make sure that the contributions from the higher order momentum compaction are small in addition.

The dynamical aperture of the lattice is computed by tracking particles with the code COSY INFINITY [201]. Initially 16 particles with the same momentum offset and having vanishing x' and y' are placed uniformly on a circle in the x-y plane. The largest radius that provides survival of the 16 particles in 1000 turns is defined here as the dynamical aperture at this momentum offset and is plotted in solid in Fig. 50 in units of the rms radius of the beam. (At the 4 cm low beta IP, the beam has an rms radius of 82 μm.) As a reference, the 7 σ aperture spanning ± 6 sigmas of momentum offset is also displayed as a semi-ellipse in dot-dashed. To maximize the aperture, first, the tunes must be chosen to avoid parametric resonances. The on-momentum amplitude dependent horizontal and vertical tunes are given in Eq. (28). With the designed rms $\epsilon_x = \epsilon_y = 0.169 \times 10^{-6}$ πm, the on-momentum tune variations are at most 0.0007. Second, the chromaticity variations with momentum must be as small as possible. This is shown in Fig. 50 (right hand side plot). Note that there are no families of sextupoles to correct for the higher order chromaticities in this small ring with only four FMC modules. As the momentum spread varies from -1 to 0.9%, ν_x varies from 8.16698 to 8.07459, and ν_y from 6.28305 to 6.22369 for the center of the beam.

During aperture tracking we notice that particle loss occurs mostly in the horizontal direction. We are convinced that the small momentum aperture is a result of the large dispersion swing in the lattice from +4.5 to -3.5 m. For example, 4.5 m dispersion and 0.6% momentum offset translates into a 2.7 cm off-axis motion. The nonlinearity of the lattice will therefore diminish the dynamical aperture. A resonant strength study using, for example, swamp plots and

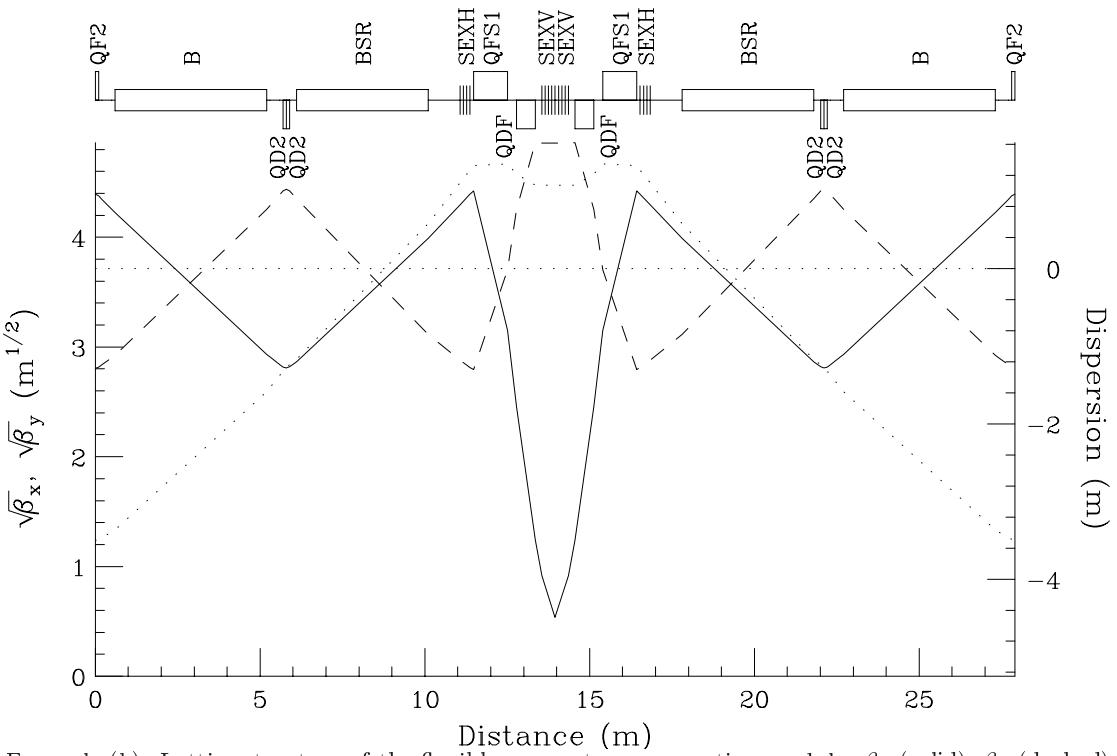

FIG. 49. Example (b): Lattice structure of the flexible momentum compaction module. β_x (solid); β_y (dashed); dispersion (dotted). The maximum and minimum β_x are 19.57 and 0.29 m, the maximum and minimum β_y are 23.63 and 7.80 m, the maximum and minimum dispersions are 1.35 and -3.50 m. The natural horizontal and vertical chromaticities are -1.77 and -0.92, giving a transition gamma of $\gamma_t = i4.43$. The total module length is 27.91 m with a total bend angle of 0.917 rad.

normalized-resonance-basis-coefficient analysis [204] actually reveals that this lattice and some of its variations are unusually nonlinear. Recently, we make a modification of the FMC arc modules which have a smaller dispersion swing from -2.6 to $+2.0$ m only. The IR has not been changed except for the matching to the arc modules. The aperture has been tracked with TEAPOT [205] in the same way as COSY and is plotted as dashed in Fig. 50 (left hand side plot). We see that the momentum aperture has widened appreciably. The dynamical aperture near on-momentum, however, is one sigma less than the lattice presented here. Nevertheless, it is not clear that this decrease is significant because all tracking has been performed in steps of one sigma only. However this type of aperture is still far from satisfactory, because so far we have been studying a bare lattice. The aperture will be reduced when fringe fields, field errors, and misalignment errors are included.

We suspect that the aperture for small momentum spread is limited by the dramatic changes in betatron functions near the IP [202]. These changes are so large that Hill's equation would no longer be adequate and the exact equation for beam transport must be used. This equation brings in nonlinearity and limits the aperture, which can easily be demonstrated by turning off all the sextupoles. In other words, although the momentum aperture can be widened by suitable deployment of sextupoles, the on-momentum dynamical aperture is determined by the triplet quadrupoles and cannot be increased significantly by the sextupoles. Some drastic changes in the low beta design may be necessary.

C. Scraping

It has been shown [206] that detector backgrounds originating from beam halo can exceed those from decays in the vicinity of the interaction point (IP). Only with a dedicated beam cleaning system far enough from the IP can one mitigate this problem [196]. Muons injected with large momentum errors or betatron oscillations will be lost within the first few turns. After that, with active scraping, the beam halo generated through beam-gas scattering, resonances and beam-beam interactions at the IP reaches equilibrium and beam losses remain constant throughout the rest of the cycle.

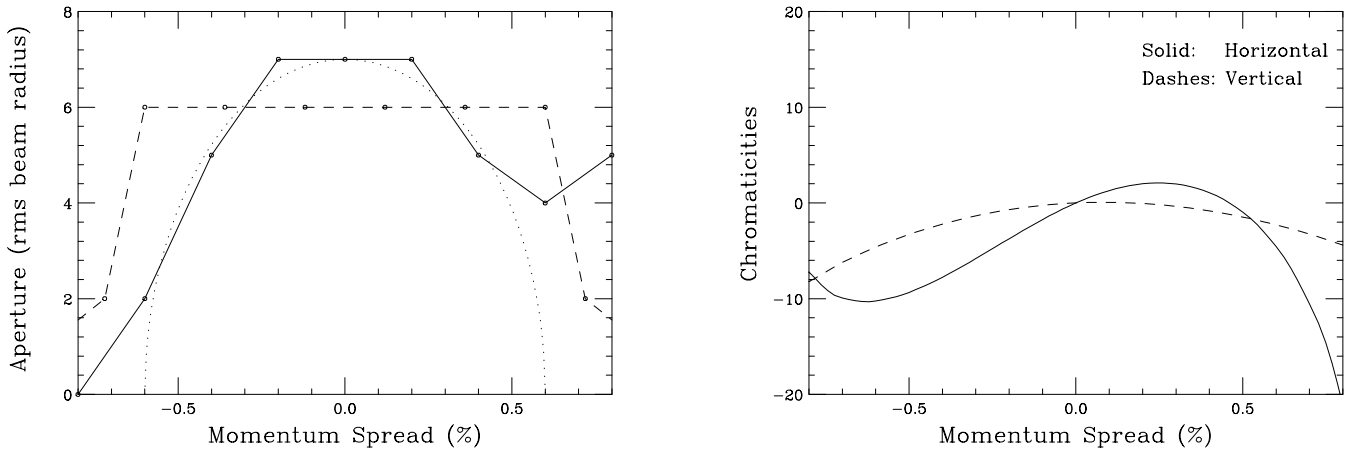

FIG. 50. Example (b): Left hand side plot is dynamical aperture of the lattice *vs.* momentum offset. COSY calculation in solid, 7 $\sigma_{\rm rms}$ in dot-dashed, and TEAPOT calculation with modified FMC modules in dashed. Right hand side plot is chromaticities *vs.* momentum offset.

Two beam cleaning schemes have been designed [196], one for muon colliders at high energies, and one for those at low energies.

The studies [196] showed that no absorber, ordinary or magnetized, will suffice for beam cleaning at 2 TeV; in fact, the disturbed muons are often lost in the IR, but a simple metal collimator was found to be satisfactory at 100 GeV.

1. Scraping for high energy collider

At high energies, a 3 m long electrostatic deflector (Fig. 51) separates muons with amplitudes larger than 3 σ and deflects them into a 3 m long Lambertson magnet, which extracts these downwards through a deflection of 17 mrad. A vertical septum magnet is used in the vertical scraping section instead of the Lambertson to keep the direction of extracted beam down. The shaving process lasts for the first few turns. To achieve practical distances and design apertures for the separator/Lambertson combinations, β functions must reach a kilometer in the 2 TeV case, but only 100 m at 50 GeV. The complete system consists of a vertical scraping section and two horizontal ones for positive and negative momentum scraping (the design is symmetric about the center, so scraping is identical for both μ^+ and μ^-). The system provides the scraping power of a factor of 1000; that is, for every 1000 halo muons, one remains.

2. Scraping for low energy collider

At 50 GeV, collimating muon halos with a 5 m long steel absorber (Fig. 52) in a simple compact utility section does an excellent job. Muons lose a significant fraction of their energy in such an absorber (8% on average) and have broad angular and spatial distributions. Almost all of these muons are then lost in the first 50-100 m downstream of the absorber with only 0.07% of the scraped muons reaching the low β quadrupoles in the IR, *i.e.* a scraping power is 1500 in this case, which is significantly better than with an earlier septum scraping system design [196] similar to that developed for the high energy collider.

D. Beam-beam tune shift

Several studies have considered beam emittance growth due to the beam-beam tune shift and none have observed significant luminosity loss. For instance, a study [207], using the high energy collider parameters (see table I), in which particles were tracked assuming Gaussian beam field distributions, and no muon decay, showed a luminosity loss of only 4%. With muon decay included, the loss contribution from beam-beam effects is even less. Another study

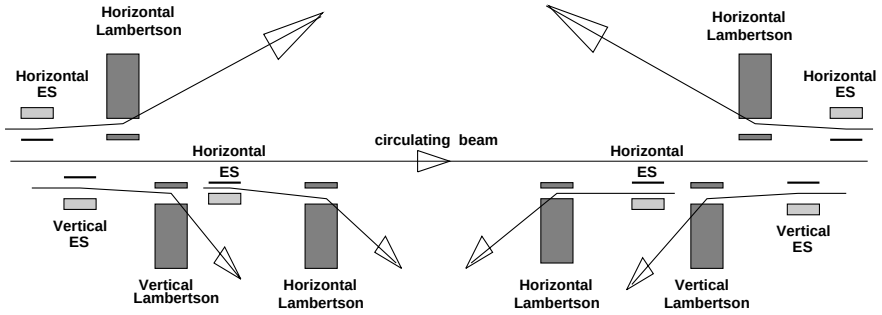

FIG. 51. Schematic view of a $\mu^+\mu^-$ collider beam halo extraction.

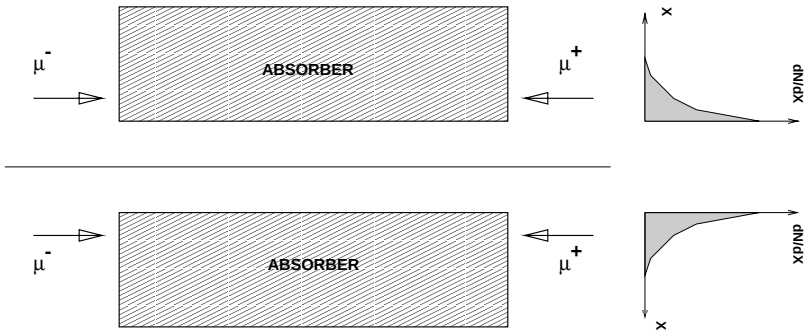

FIG. 52. Scraping muon beam halo with a 5 m steel absorber.

[208] using a particle in cell approach with no assumptions about field symmetry obtained a similar result. Collisions between beams displaced by 10% of their radius also gave little loss. But all these studies assumed an ideal lattice, and none considered whether small losses due to nonlinearities give rise to an unacceptable background.

E. Impedance/wakefield considerations

A study [209] has examined the resistive wall impedance longitudinal instabilities in rings at several energies. At the higher energies and larger momentum spreads, solutions were found with small but finite momentum compaction and moderate rf voltages. For the special case of the Higgs Factory, with its very low momentum spread, a solution was found with no synchrotron motion, but rf was provided to correct the first order impedance generated momentum spread. The remaining off-momentum tails which might generate background could be removed by a higher harmonic rf correction without affecting luminosity. Solutions to the higher energy and larger momentum spread cases without synchrotron motion are also being considered.

Given the very slow or nonexistent synchrotron oscillations, the transverse beam breakup instability is significant. This instability can be stabilized using rf quadrupole [189] induced BNS damping. For instance, the required tune shift with position in the bunch, calculated using the two particle model approximation [210], is only 1.58×10^{-4} for the 3 TeV case using a 1 cm radius aluminum pipe. This stabilizes the resistive wall instability. However, this application of BNS damping to a quasi-isochronous ring, and other head-tail instabilities due to the chromaticities ξ and η_1, needs more study.

F. Bending magnet design

The dipole field assumed in the 100 GeV collider lattices described above was 8 T. This field can be obtained using 1.8^o niobium titanium (NbTi) *cos theta* superconducting magnets similar to those developed for the LHC. The only complication is the need for a tungsten shield between the beam and coils to shield the latter from beam decay heating.

The μ's decay within the rings ($\mu^- \rightarrow e^-\overline{\nu_e}\nu_\mu$), producing electrons whose mean energy is approximately 0.35 that of the muons. With no shielding, the average power deposited per unit length would be about 2 kW/m in the 4 TeV

machine, and 300 W/m in the 100 GeV Higgs factory. Figure 53 shows the power penetrating tungsten shields of different thickness [44,195,196,211]. One sees that 3 cm in the low energy case, or 6 cm at high energy would reduce the power to below 10 W/m, which can reasonably be taken by superconducting magnets.

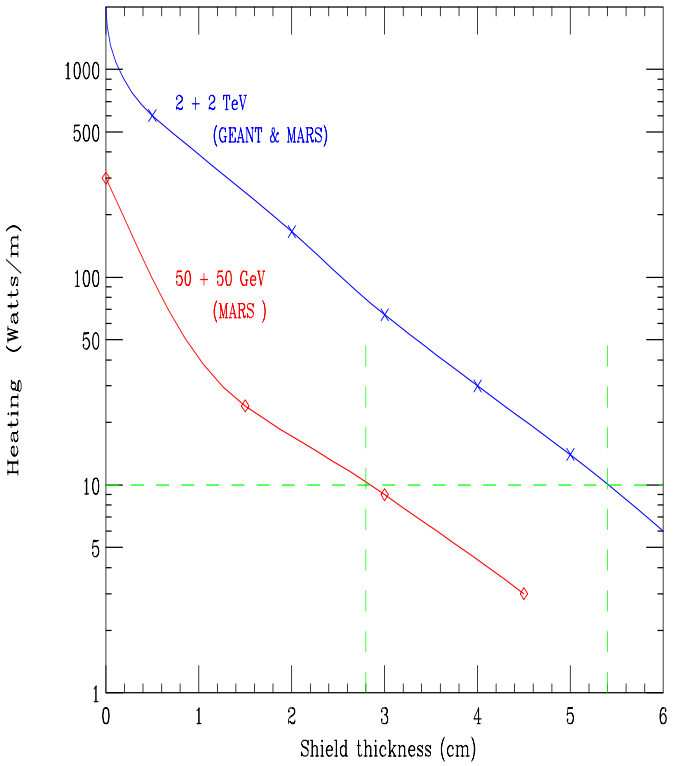

FIG. 53. Power penetrating tungsten shields vs. their thickness for a) 4 TeV, and b) 0.1 TeV, colliders.

Figure 54 shows the cross section of a baseline magnet suitable for the 100 GeV collider.

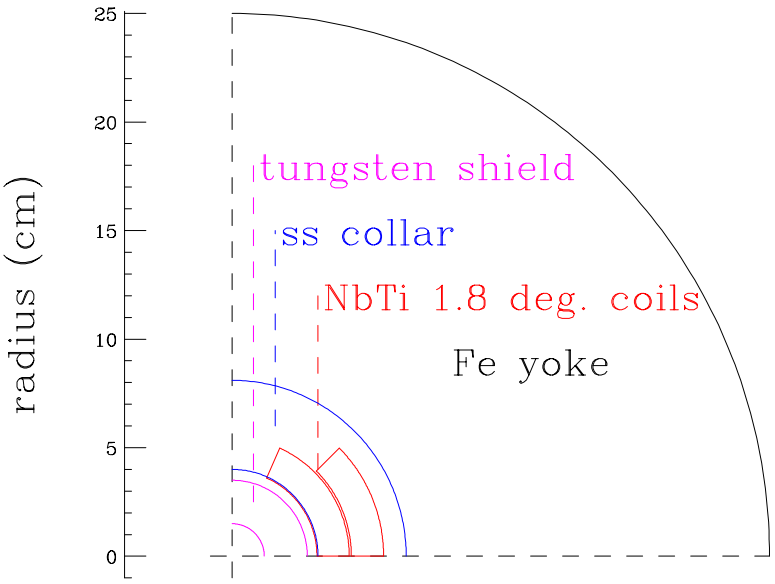

FIG. 54. Cross Section of a baseline dipole magnet suitable for the 100 GeV collider.

The quadrupoles could use warm iron poles placed as close to the beam as practical. The coils could then be either superconducting or warm, placed at a greater distance from the beam and shielded from it by the poles.

The collider ring could be made smaller, and the luminosity increased, if higher field dipoles were used. In the low energy case, the gain would not be great since less than half the circumference is devoted to the arcs. For this

reason, and to avoid yet another technical challenge, higher field magnets are not part of the baseline design of a 100 GeV collider. But they would give a significant luminosity improvement for the higher energy colliders, and would be desirable there. There have been several studies of possible designs, three of which (two that are promising and one that appears not to work) are included below.

1. Alternative racetrack Nb_3Sn dipole

A higher field magnet based on Nb_3Sn conductor and racetrack coils is presently being designed. The Nb_3Sn conductor allows higher fields and provides a large temperature margin over the operating temperature, but being brittle and sensitive to bending or other stress, presents a number of engineering challenges.

In this design, the stress levels in the conductor are reduced by the use of a rectangular coil block geometry and end support problems are reduced by keeping the coils flat. In the more conventional *cos theta* designs, the conductor is distributed around a cylinder and the forces add up towards the midplane; in addition, the ends, as they arc over the cylinder, are relatively hard to support.

The geometry of the cross section is shown in Fig. 55. It uses all 2-D flat racetrack coils. Each quadrant of the magnet aperture has two blocks of conductors. The block at the pole in the first quadrant has a return block in the second quadrant, similar to that in a conventional design. The height of this block is such that it completely clears the bore. In a conventional design, the second block, the midplane block, would also have a return block in the second quadrant. That would, however, require the conductor block to be lifted up in the ends to clear the bore and thus would lose the simple 2-D geometry. In the proposed design, the return block retains the 2-D coil geometry, as it is returned on the same side (see Fig. 55) and naturally clears the bore. Since the return block does not contribute to the field, this design uses 50% more conductor. This, however, is a small penalty to pay for a few magnets where the performance and not the cost is a major issue. The field lines are also shown in Fig. 55.

Preliminary design parameters for two cases are given in table XIII. The first case is one where the performance of the cable used is the same that is in the LBL D20 magnet, which created a central field of 13.5 T. The second case is the one where the cable is graded and two types of cable are used, and it is assumed that a reported improvement in cable performance is realized. It is expected to produce a central field of 14.7 T when operated at 4.2 ^oK.

TABLE XIII. Preliminary design parameters for a racetrack Nb_3Sn dipole with two different types of cable.

Case 1: Same conductor as in LBL 13.5 T D20 magnet without grading	
Central field at quench	13 T at 4.2 ^oK
Coil dimensions	25 mm × 70 mm
Total number of racetrack coils in whole magnet	6
Total number of blocks per quadrant in aperture	2 (+1 outside the aperture)
Yoke outer radius	500 mm (same as in D20)
Field harmonics	a few parts in 10^{-5} at 10 mm
Midplane gap (midplane to coil)	5 mm (coil to coil 10 mm)
Minimum coil height in the end	45 mm (Note: coils are not lifted up.)
Case 2: Newer conductor and graded	
Central field at quench	14.7 T at 4.2 ^oK
Grading	70 mm divided in two 35 mm layers
Overall current densities	370 A/mm^2 and 600 A/mm^2
Peak fields	16 T and 12.5 T
Copper current density	1500 A/mm^2
Other features are the same as in *Case 1*	

2. Alternative Cos Theta Nb_3Sn dipole

In this case the problem with the brittle and sensitive conductor is solved by winding the coil inside many separate slots cut in metal support cylinders. There is no build up of forces on the coil at the mid-plane. The slots continue around the ends, and thus solve the support problem there too.

Figure 56 shows this alternative Nb_3Sn dipole *cos theta* design. It is an extension of the concept used to build helical magnets [212] for the polarized proton program at RHIC [213]. The magnet is wound with pre-reacted, kapton-insulated, B-stage impregnated, low current cable. The build up of forces is controlled by laying the cables

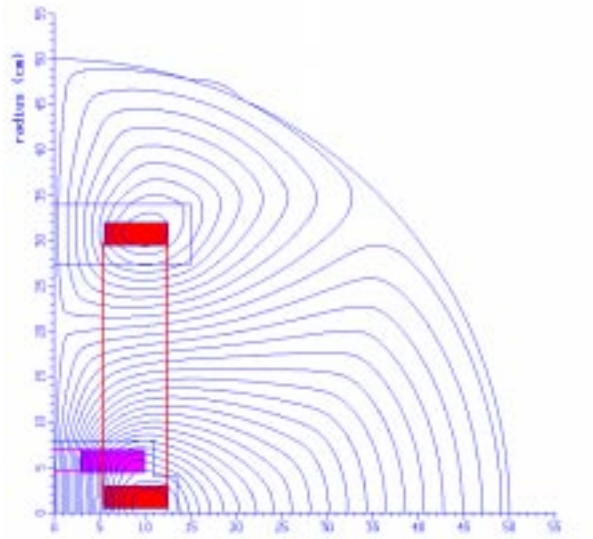

FIG. 55. Cross section of alternative high field ($\approx$ 15 T) race track coil dipole magnet with Nb_3Sn conductor.

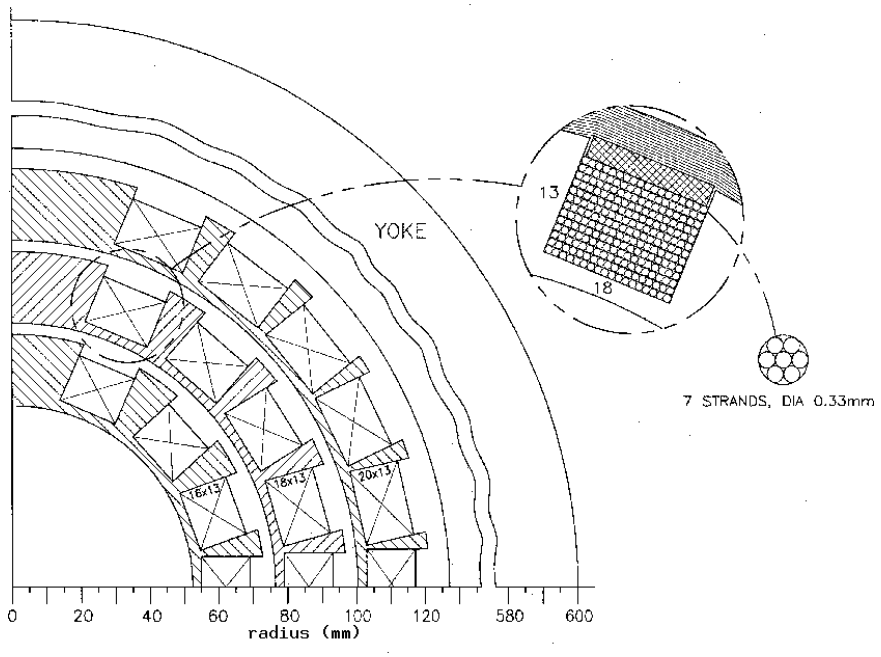

FIG. 56. Cross section of alternative high field slot dipole made with Nb_3Sn conductor.

in machined slots in a metal support cylinder. After winding, the openings of the slots are bridged by metal spacers and the coils pre-compressed inward by winding B-stage impregnated high tensile thread around the spacers. After curing, the outside of each coil assembly is machined prior to its insertion into an outer coil, or into the yoke. There are 3 layers. The inner bore is 55 mm radius, the outer coil radius approximately 118 mm, and the yoke inside radius is 127 mm. The maximum copper current density is 1300 A/mm^2.

Using the same material specifications as used in the above high field option, a central short sample field of 13.2 T was calculated. This is somewhat less than the block design discussed above, but could be improved by increasing the cable diameters to improve the currently rather poor (64%) cable to cable-plus-insulator ratio.

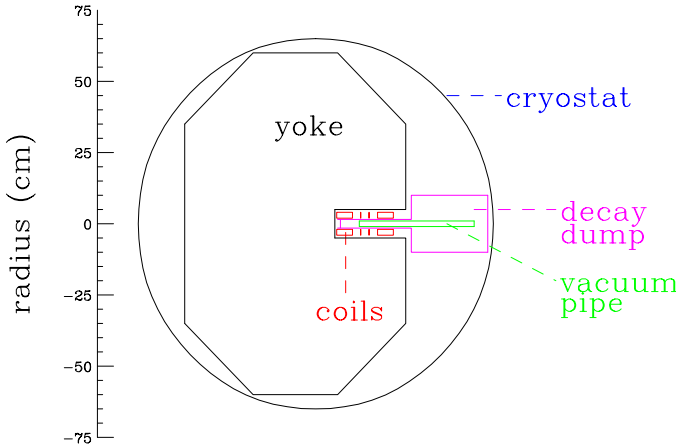

FIG. 57. Cross section of an unsuccessful alternative high field C magnet with open mid-plane.

Figure 57 shows the cross section of a high field dipole magnet in which it was hoped to bring the coils closer to the beam pipe without suffering excessive heating from beam decay. The coil design [214] appeared reasonable, but the required avoidance of coil heating was not achieved.

Decay electrons are generated at very small angles ($\approx\ 1/\gamma$) to the beam, and with an average energy about 1/3 of the beam. Such electrons initially spiral inward (to the right in Fig. 57) bent by the high dipole field. In the high energy case, these electrons also radiate a significant fraction of their energy as (≈ 1 GeV) synchrotron gamma rays, some of which end up on the outside (to the left in Fig. 57). The concept was to use a very wide beam pipe, allow the electrons to exit between the coils, and be absorbed in an external cooled dump. Unfortunately a preliminary study found that a substantial fraction of the electrons did not reach the dump. They were bent back outward before reaching it by the return field of the magnet coils and the nature of the curved ring geometry. Such electrons were then trapped about the null in the vertical field and eventually hit the upper or lower face of the unshielded vacuum pipe. They showered, and deposited unacceptable levels of heat in the coils.

Another idea called for collimators between each bending magnet that would catch such trapped electrons. This option has not been studied in detail, but the impedance consequences of such periodic collimators are expected to be unacceptable.

Further study of such options might find a solution, but the use of a thick cylindrical heavy metal shield appears practical, adequate, and is thus the current baseline choice.

G. Energy scale calibration

In order to scan the width of a Higgs boson of mass around 100 GeV, one needs to measure the energy of the individual muon stores to an accuracy of a few parts per million, since the width of a Higgs boson of that mass is expected to be a few MeV. Assuming that muon bunches can be produced with modest polarizations of ≈ 0.25, and that the polarization can be maintained from turn to turn in the collider, it is possible to use the precession of the polarization in the ring to measure accurately the average energy of the muons [12]. The total energy of electrons produced by muon decay observed in the calorimeter placed in the ring varies from turn to turn due to the $g-2$ precession of the muon spin, which is proportional to the Lorentz factor γ of the muon beam. Figure 58 shows the result of a fit of the total electron energy observed in a calorimeter to a functional form that includes muon decay and spin precession. Figure 59(a) shows the fractional error $\delta\gamma/\gamma$ obtained from a series of such fits plotted against the fractional error of measurement in the total electron energy that depends on the electron statistics. It has been shown that precisions of a few parts per million in γ are possible with modest electron statistics of $\approx 100,000$ detected. It should be noted that there are 3.2×10^6 decays per meter for a muon intensity of 10^{12} muons. Figure 59(b) shows the fractional error in $\delta\gamma/\gamma$ obtained by fitting the rate of decay of the muons in the collider. The accuracy using this method is much worse than that from fitting the polarization oscillation and cannot be used for precision measurement of the energy. Figure 59(c) shows the χ^2 of the fits. No significant fitting biases are evident.

Our current plans to measure the energy due to decay electrons entail an electromagnetic calorimeter that is segmented both longitudinally and transversely and placed inside an enlarged beam pipe in one of the straight

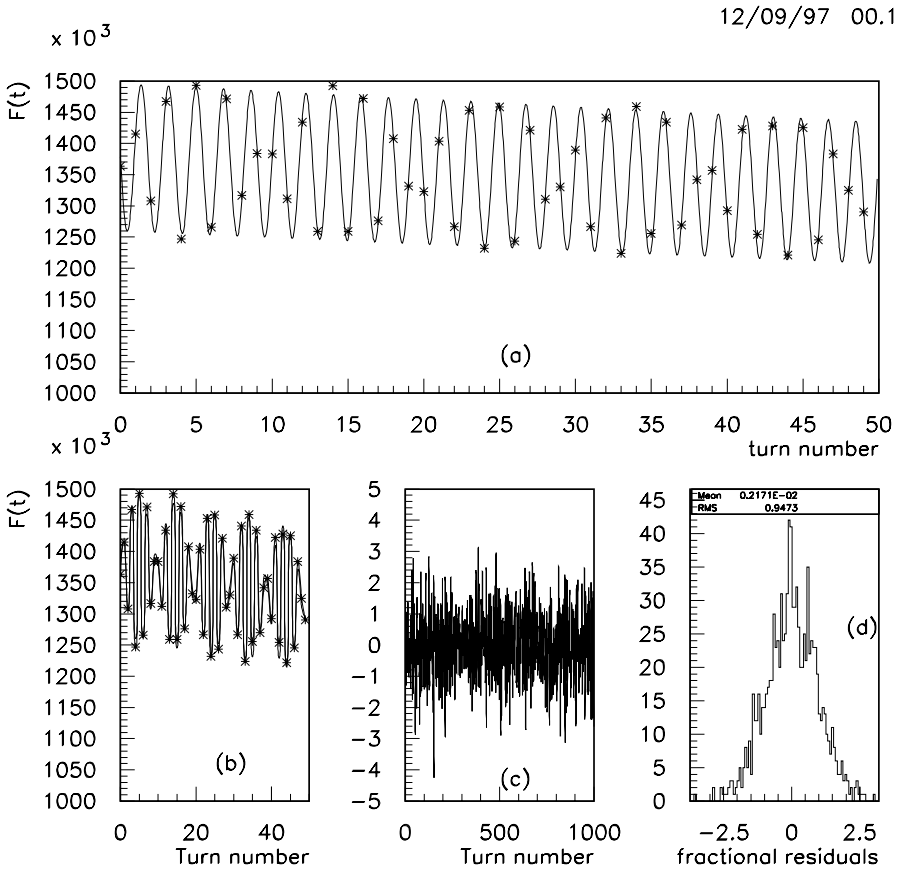

FIG. 58. a) Energy detected in the calorimeter during the first 50 turns in a 50 GeV muon storage ring (points). An average polarization value of $\hat{P} = -0.26$ is assumed and a fractional fluctuation of 5×10^{-3} per point. The curve is the result of a MINUIT fit to the expected functional form. b) The same fit, with the function being plotted only at integer turn values. A beat is evident. c) Pulls as a function of turn number. d) Histogram of pulls. A pull is defined by (measured value-fitted value)/(error in measured-fitted).

sections in the collider ring. The length of the straight section upstream of the calorimeter can be chosen to control the total number of decays and hence the rate of energy deposition. The sensitive material can be gaseous, since the energy resolution is controlled by decay fluctuations rather than sampling error. In order to measure the total number of electrons entering the calorimeter, we plan to include a calorimeter layer with little absorber upstream of it as the first layer.

This scheme will enable us to calibrate and correct the energy of individual bunches of muons and permit us to measure the width of a low mass Higgs boson.

VIII. RADIATION AND BACKGROUNDS

A. Conventional radiation

The proton source generates a 4 MW proton beam, which is comparable to the proposed spallation source [92]. This is a very high power and will, as in the spallation source, require great care in reducing unwanted particle losses, as well as careful machine shielding, and target and beam dump design. Initial studies of the target and capture solenoid region have been performed with the MARS code, and preliminary specifications for shielding determined, but more work is needed.

The cooling and accelerator chain is rather clean, since a relatively small fraction of the muons decay, and their energies are low. Power deposited in the accelerators is typically 10-30 W/m (see table IX and table X).